Investigating the Cytotoxic Redox Mechanism of PFOS within Hep G2 by Hyperspectral Assisted-Scanning Electrochemical Microscopy

Journal:	*Analyst*
Manuscript ID	AN-ART-05-2022-000904.R1
Article Type:	Paper
Date Submitted by the Author:	30-Jun-2022
Complete List of Authors:	Goines, Sondrica; The University of North Carolina at Chapel Hill, Chemistry Dick, Jeffrey; The University of North Carolina at Chapel Hill, Chemistry

Investigating the Cytotoxic Redox Mechanism of PFOS within Hep G2 by Hyperspectral Assisted-Scanning Electrochemical Microscopy

Sondrica Goines[a] and Jeffrey E. Dick[a, b]*

[a]Department of Chemistry, The University of North Carolina at Chapel Hill, Chapel Hill, NC 27599, USA
[b]Lineberger Comprehensive Cancer Center, The University of North Carolina at Chapel Hill, Chapel Hill, NC 27599, USA
*To whom all correspondence should be addressed: jedick@email.unc.edu

Abstract

Perfluorooctane sulfonate (PFOS) is one of the most lethal per- and poly-fluoroalkyl substances (PFAS). Generally, exposure effects are studied through case-controlled studies, cohort studies, or cell assays. Unfortunately, most studies involving two-dimensional cell cultures require cell lysis or fixation. For *in vitro* studies, fluorescence microscopy has been useful, but methods to simultaneously discern phototoxicity effects during an experiment are limited. Here, we use hepatocarcinoma (Hep G2) cells to examine the redox mechanism of PFOS cytotoxicity *in vitro,* while using a hyperspectral assisted-scanning electrochemical microscope to differentiate between PFOS and redox mediator induced stress. Specifically, we correlate an increase in the electrochemical response of ferrocenemethanol oxidation with an increase in intracellular reactive oxygen species (ROS). Hyperspectral imaging of redox active-fluorophores implicates superoxide in the cytotoxic redox mechanism.

Introduction

Labeled 'forever chemicals' based on characteristic networks of strong C – F bonds, manufactured per- and poly-fluoroalkyl substances (PFAS) are used in the production of a variety of daily-use consumer goods.[1] Global production and use of PFAS since the 1940s has resulted in the contamination of food, beverages, and waterways worldwide.[2] Unfortunately, PFAS display strong binding capacities for serum albumin, phospholipids, and fatty acid binding proteins inevitably causing health risks.[3, 4] For example, perfluorooctanoic acid (PFOA) and perfluorooctane sulfonate (PFOS) may establish two and three hydrogen bonds, respectively, with human liver-fatty acid binding protein between the carboxyl head of the PFAS and amino acid residues of the protein.[4] Moreover, the properties that make PFAS useful – such as high thermal stability, chemical stability, and surfactant activity – are the culprits responsible for various health concerns associated with exposure (*i.e.,* infertility[5], kidney and testicular cancers[6], and liver and kidney disease[7]).[2]

Prior to 2002, PFOS was one of the most widely used PFAS in the United States until the polymer's adverse health effects became evident. Case-controlled and cohort studies near regions of high contamination presented exposure as an occupational hazard as well as a public health concern.[2, 8-11] Quantifiable concentrations of PFOS were reported in bodily fluids (*i.e.,* blood, milk, and urine), hair, and nails.[2] With a half-life greater than five years, PFOS may be retained in human tissue for prolonged periods of time. Bioaccumulation studies report PFOS in the brain, lungs, kidneys, and liver with the micropollutant being dominant in the liver, making hepatoxicity studies a relevant area of focus.

Recent studies have investigated cytotoxicity, cell proliferation, and bioaccumulation of PFOS through colorimetric and fluorescence viability assays, flow cytometry, qPCR, and mass spectrometry.[3-5, 12-17] Unfortunately, these studies generally rely on cell lysis or fixation limiting our ability to probe metabolism as a function of time. Very few techniques are readily accessible to probe the mechanism of cytotoxicity in living cells *in vitro*, while accounting for cell-to-cell heterogeneity and the heterogeneity of intracellular material.[18, 19] While fluorescence microscopy is minimally destructive, this method may have phototoxic effects on cellular respiration.[20] However, electrochemical techniques that use nano- and micro-electrodes have been used to examine living cells in real time with minimal perturbation to cellular homeostasis.[21-23] Additionally, electrochemistry has become more appealing to those constructing diagnostic technologies since decreasing electrode size enables one to detect a single entity (*i.e.,* a single cell, organelle, or biomolecule) within seconds.[24]

Here, we use electrochemical imaging to investigate the mechanism of PFOS cytotoxicity within living cells *in vitro*. Scanning electrochemical microscopy (SECM) – a scanning probe technique used to characterize local topography and reactivity – has been used in a variety of bioanalytical investigations because it is inherently non-invasive and provides high spatial and temporal resolution.[21] With the use of membrane permeable, hydrophobic redox mediators, SECM has been used to examine variations in the cellular redox state. For example, neutral, ferrocene derivatives[25, 26] and menadione[27] are often used to examine the cellular redox state as a function of glutathione. In particular, SECM is useful when examining cellular response to stimuli. Previously, SECM has been used to image changes in cellular respiration[28-30], the secretion of proteins[31, 32], and transmembrane protein activity[33]. Biological SECM platforms are typically composed of a traditional SECM piezoelectric positioner mounted on an inverted, fluorescence microscope. These platforms allow users to differentiate between cells and investigate redox activity *via* fluorescence and electrochemical microscopy.

Hyperspectral assisted-SECM has the potential to elucidate redox mechanisms responsible for an electrochemical response by offering validation through three forms of data: electrochemical, optical, and spectral data.[34] Previously, we demonstrated the use of variable fluorescence bandpass hyperspectral imaging in combination with SECM by showing the technique's ability to discern between extra- and intra-cellular boundaries within a two-dimensional co-culture system.[34] This previous investigation did not make use of redox active-fluorophores, limiting our insight into the redox mechanism responsible for the observed electrochemical response. Here, we use hyperspectral assisted-SECM to investigate the redox mechanism for PFOS cytotoxicity using hepatocarcinoma (Hep G2) cells. Hep G2 cells are often used as a model within pharmaceutical, cytotoxicity studies based on comparable phase II enzyme activity between Hep G2 and normal hepatocytes. Phase II enzymes, such as glutathione-*S*-transferase, are responsible for catalyzing conjugation reactions involved in regulatory processes following oxidative stress.[35] Additionally, PFOS exposure has been implicated in hepatotoxicity *via* lipid accumulation.[17, 36] Specifically, hyperspectral assisted-SECM is used to distinguish between PFOS exposure effects and mediator induced stress in real time. This manuscript aims to build a framework for the electrochemical characterization of cytotoxic redox mechanisms with minimal perturbation to cellular homeostasis. While this investigation is specific to exposure to PFOS, it presents a generalizable method of study for toxicology research.

Experimental

Reagents and Materials

Hepatocarcinoma (Hep G2) cells were obtained from the University of North Carolina at Chapel Hill. Cells were maintained using Dulbecco's Modified Eagle's Medium (DMEM) – high glucose (with 4500 mg L^{-1} glucose, L-glutamine, sodium pyruvate, and sodium bicarbonate) supplemented with 10% v/v fetal bovine serum (FBS), 2.5% v/v 1 M HEPES buffer (sterile, pH 7.3), and 1% v/v penicillin-streptomycin (*i.e.,* full growth media). DMEM – high glucose was purchased from Sigma-Aldrich. Premium grade 100% FBS and 1 M HEPES buffer were purchased from VWR International, LLC. Gibco^{TM} Dulbecco's phosphate buffered saline (DPBS, 1X, pH 7.4) and Gibco^{TM} TrypLE Express were purchased from Thermo Fisher Scientific. Cells were cultured in 10 cm-diameter and 3.5 cm-diameter attachment treated tissue culture dishes purchased from VWR International, LLC.

For electrochemical methods, hydroxymethylferrocene (ferrocenemethanol, $FcCH_2OH$, 97%) was purchased from Alfa Aesar. For fluorescence imaging, 2',7'-dichlorofluorescin diacetate (DCF-DA, ≥97%) and monochlorobimane (MBCl, ≥70%), were purchased from Sigma-Aldrich. Glutathione (GSH) and superoxide dismutase 1 inhibitor (SOD1 inhibitor, LCS-1) were purchased from Sigma-Aldrich. Dimethyl sulfoxide (DMSO) was purchased from VWR International, LLC. All reagents were used without further purification.

Instrumentation

Correlated scanning electrochemical microscopy, optical/fluorescence microscopy, and hyperspectral imaging were obtained using variable fluorescence bandpass hyperspectral imaging system coupled to a bipotentiostat; a schematic representation of the system, **Scheme S1**, is featured in the **Electronic Supporting Information** (**ESI**).[34] The imaging system contains a Leica DMi8 inverted microscope and a Leica DFC7000 GT monochrome digital camera, both controlled by a Lecia CTR advanced electronics box. The microscope motorized stage is controlled by a Leica SP box (Leica Microscope Systems, Germany). To obtain hyperspectral images with the Leica digital camera, the system is equipped with a Lambda LS xenon arc lamp as a white light source and two Lambda VF-5^{TM} tunable filter changers; to select excitation and emission wavelengths, each filter changer is equipped with five VersaChrome® tunable filters made by Semrock (**Table S1**). Lambda equipment is controlled by a Lambda 10-3 controller and a Lambda SC *Smart*Shutter^{TM}; all Lambda equipment were purchased from Sutter Instrument Company (Novato, CA). Additionally, a custom 80/20 beam splitter is engaged for hyperspectral or fluorescence imaging when using the Lambda equipment and the Leica digital camera. For imaging in bypass mode (*i.e.,* when the Lambda equipment is not engaged and standard microscope equipment is in use) conventional GFP, TXR, Y5, and DAPI filter cubes (Leica Microscope Systems, Germany) may be used in combination with an ORCA-fusion BT digital camera C15440 (Hamamatsu Photonics K. K., Hamamatsu City, Japan).

For correlated electrochemical imaging, the condenser and bright field light source of the inverted microscope were replaced with the stepper and piezoelectric positioner of a 920D bipotentiostat (CH Instruments, Inc., Austin, TX). Electrochemical images were captured using a Pt microelectrode tip ($r = 5$ µm, RG ≤ 2), a Ag/AgCl (1 M KCl) reference electrode, and a glassy carbon rod counter electrode ($r = 1.5$ mm). The microelectrode and reference electrode were purchased from CH Instruments, Inc. (Austin, TX), and the counter electrode was purchased from Alfa Aesar. Electrochemical imaging was performed using a salt bridge prepared with 1 M KCl suspended in agarose. For electrochemical methods in bulk solution, a Pt macroelectrode ($r = 1$ mm) was purchased from CH Instruments, Inc. (Austin, TX).

Cells were incubated at 37 °C and 5% CO_2 within a Heracell VIOS 160i CO_2 incubator purchased from Thermo Fisher Scientific. Additionally, cells were counted using an automated Corning Cell Counter and the associated CytoSMART application purchased from CytoSMART Technologies, LLC (Skillman, NJ).

Hyperspectral assisted-scanning electrochemical microscopy of Hep G2 following PFOS exposure: reactive oxygen species content analysis

Hep G2 P20 cells were cultured in full growth media within 3.5 cm-diameter tissue culture dishes. At 75% to 80% confluence (*i.e.,* medium to high density), spent media was removed from the dishes and the cells were rinsed with 1 mL DPBS. Next, 2 mL solutions of 0, 50, and 100 µM PFOS-supplemented full growth media were added to the dishes to prepare a sample for each concentration of PFOS. Each dish was labeled based on the concentration of PFOS added, then placed in the incubator.

After incubating the cells for 16 hours overnight, spent PFOS-supplemented full growth media was removed from the dishes. To analyze the intracellular reactive oxygen species (ROS) content, the cells were rinsed with 1 mL DPBS and loaded with 1 mL 10 µM DCF-DA in DPBS for 10 minutes in the dark at room temperature. After, cells were rinsed with 1 mL DPBS, then 2 mL full growth media was added to each dish before placing them in the incubator for later use.

Prior to imaging, tilt correction was performed (**Figure S3**). Next, spent media was removed from the 100 µM PFOS sample and the cells were rinsed with DPBS before adding 0.5 mM $FcCH_2OH$ in DPBS to the sample dish. After placing the dish on the microscope stage, three electrodes were placed in solution: a salt bridge to an external Ag/AgCl (1 M KCl) reference electrode in DPBS, a glassy carbon rod counter electrode ($r = 1.5$ mm), and a Pt microelectrode tip ($r = 5$ µm) using a 3D printed holder attached to the piezoelectric positioner of the 920D bipotentiostat. Next, cells were brought into focus in bright field using a 20× objective lens, then the Pt microelectrode tip was used to approach cells at +0.5 V vs. Ag/AgCl (**Figure S4**). After obtaining a feedback response and observing cell movement, the Pt microelectrode tip was moved upward 10 µm until no cell movement was observed.

Next, a fluorescence image of dichlorofluorescein (DCF), indicative of ROS content, was captured at $\lambda_{ex}/\lambda_{em}$ 495/535 nm using the hyperspectral system. The system was then used to obtain a two-dimensional stack of images obtained at multiple emission wavelengths with a single excitation wavelength from the emission of 535 nm to 550 nm with a step size of 1 nm at an excitation of 495 nm (**Figure S5i**). A corresponding electrochemical image was obtained with the Pt microelectrode tip at +0.5 V vs. Ag/AgCl approximately one hour after adding the redox mediator solution to the cell culture dish. This incubation period allowed passive diffusion of $FcCH_2OH$ into the cells.[33] Electrochemical imaging was completed at a working distance ≤10 µm to maintain an appropriate working distance (*i.e.,* $d \leq 2a$, where d is the working distance from the substrate and a is the radius of the electrode tip) while avoiding tip-to-sample crashes that may be observed when imaging large aspect ratio samples; this technique has been used previously when imaging cell samples[37]. This series of imaging steps was repeated with samples exposed to 50 µM and 0 µM PFOS. All electrochemical, optical, and spectral data are shown in **Figure S5**.

A detailed experimental method for hyperspectral assisted-scanning electrochemical microscopy of Hep G2 cells loaded with DCF-DA is provided in the **ESI**. Additionally, a cell viability study shown in the **ESI** confirmed that Hep G2 cells remain >95% viable and adequate to use to evaluate activity post PFOS exposure (**Figure S6**).

Scanning electrochemical microscopy of Hep G2 following PFOS exposure: variation in cellular reactivity over time

Hep G2 P23 cells were cultured in full growth media within 3.5 cm-diameter tissue culture dishes. At 75% to 80% confluence, spent media was removed from the dishes and the cells were rinsed with 1 mL DPBS. Next, 2 mL solutions of 0 and 100 µM PFOS-supplemented full growth media were added to dishes to prepare samples for each concentration. Each dish was labeled based on the concentration of PFOS added, then placed in the incubator.

After incubating the cells for 48 hours, spent PFOS-supplemented full growth media was removed from the dishes. Next, cells were rinsed with 1 mL DPBS, then 2 mL full growth media was added to each dish before placing them in the incubator for later use.

For electrochemical imaging, spent media was removed from a 100 µM PFOS sample and the cells were rinsed with DPBS before adding 0.5 mM $FcCH_2OH$ in DPBS to the sample dish. Cells were brought into focus in bright field using a 20× objective lens, then electrochemically imaged as done previously. After the initial image, a second image was captured every hour for two additional hours at the same *xy* and *z* positions. Lastly, an optical image of the imaged region was captured. This imaging procedure was repeated for the 0 µM PFOS sample.

Ferrocenium methanol reduction *via* glutathione

To provide evidence for ferrocenium methanol (Fc^+CH_2OH) reduction *via* GSH production at the cell membrane, the hypothesized redox mechanism was investigated in bulk solution using cyclic voltammetry.

Solutions of 0.5 mM GSH and $FcCH_2OH$ were prepared in DPBS. After purging each solution with argon gas for 5 minutes, initial voltammograms were obtained with a three-electrode system similar to that used in the microscopy experiments: a Pt macroelectrode (r = 1 mm), a Ag/AgCl (1 M KCl) reference electrode, and a glassy carbon rod counter electrode (r = 1.5 mm). To obtain the voltammograms, the Pt macroelectrode was scanned from 0 V to +0.5 V vs. Ag/AgCl at 0.2 V/s, then in the reverse direction based on the potential range for the reversible oxidation of $FcCH_2OH$. These controls are shown in polarographic convention in **Figure S7**.

Next, five solutions of 0.5 mM $FcCH_2OH$ were prepared containing 0 mM, 0.5 mM, 1.0 mM, 2.0 mM, and 4.0 mM GSH in DPBS. After purging each solution with argon gas for 5 minutes, a voltammogram was captured in each solution. Between each voltammogram, the Pt macroelectrode was polished using 1.0 mm, 0.3 mm, and 0.05 mm alumina powder, in succession, then rinsed with ultrapure water.

Hyperspectral imaging of Hep G2 following PFOS exposure: glutathione contribution analysis

Hep G2 P19 cells were cultured in full growth media within 3.5 cm-diameter tissue culture dishes. At ≤50% confluence (*i.e.,* medium density), spent media was removed from dishes and the cells were rinsed with 1 mL DPBS. Next, 2 mL solutions of 0, 50, and 100 μM PFOS-supplemented full growth media were added to the dishes to prepare one sample for each PFOS concentration.

After incubating the cells for 16 hours overnight, spent PFOS-supplemented full growth media was removed from the dishes. The cells were loaded with 10 μM DCF-DA as done previously. Next, 2 mL 0.5 mM $FcCH_2OH$/20 μM MBCl in DPBS was added to each dish. To analyze GSH content, fluorescence images were obtained at an excitation of 390 nm and an emission of 490 nm (*i.e.,* an emission indicative of the MBCl-GSH conjugate) using the hyperspectral imaging platform. Additional spectral data was captured using the hyperspectral imaging platform. An example spectrum is provided in **Figure S8**. Mean emission intensities at 490 nm were averaged over three distinct regions of interest ($N = 3$) to produce data presented in main text.

Hyperspectral assisted-scanning electrochemical microscopy of Hep G2 following exposure to PFOS: SOD1 contribution analysis

Hep G2 P28 cells were cultured in 3.5 cm-diameter tissue culture dishes using full growth media. At 60 to 65% confluence, spent media was removed from the dishes and the cells were rinsed with 1 mL DPBS. To inhibit superoxide dismutase 1 (SOD 1), cells were incubated in 5 μM LCS-1 in DPBS in the dark at room temperature for 15 minutes. After inhibition of SOD 1, the cells were rinsed with 1 mL DPBS. Next, 2 mL of 0 and 100 μM PFOS-supplemented full growth media was added to the dishes to prepare multiple samples for each concentration.

After incubating cells for 16 hours overnight, spent media was removed from the dishes. Next, the cells were loaded with 10 μM DCF-DA as done previously. Finally, the dishes were imaged in 0.5 mM $FcCH_2OH$ in DPBS as done previously. Fluorescence images obtained using the hyperspectral system used an excitation of 495 nm and an emission of 535 nm.

Results and discussion

Following exposure to perfluorooctane sulfonate (PFOS) for 15 hours, hepatocarcinoma (Hep G2) cells were reported to have significantly higher reactive oxygen species (ROS) content *via* dichlorofluorescein (DCF) fluorescence imaging.[17] To ensure significant PFOS exposure effects on ROS content and initialize the cytotoxic mechanism, Hep G2 cells were exposed to 0, 50, and 100 μM PFOS for at least 16 hours, then loaded with 2', 7'-dichlorofluorescin diacetate (DCF-DA). DCF-DA is a membrane permeable substance that reacts with intracellular esterases to release esterified acids and react with intracellular ROS to fluoresce as DCF.[38] After electrochemically imaging Hep G2 cells – previously exposed to PFOS and loaded with DCF-DA – in the presence of ferrocenemethanol ($FcCH_2OH$), an increase in the electrochemical response was observed as a function of PFOS concentration (**Figure 1a & 1c**). Here, it is important to note that the electrochemical response is normalized by the limiting current (*i.e.,* $i_{T,\infty}$ when $d >> 10a$, where d is the distance from the substrate and a is the electrode radius) for direct comparison of electrochemical images regardless of variations in tip-to-substrate distance. In addition, fluorescence images validated literature precedent as the emission intensity of DCF increased as a function of PFOS concentration (**Figure 1b & 1d**). These data demonstrate an increase in cellular redox activity as a function of PFOS exposure, with this increase being seemingly related to intracellular ROS content.

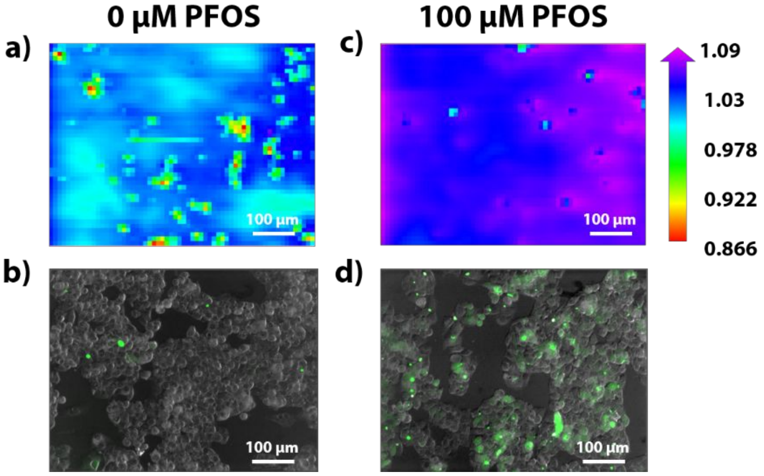

Figure 1. Correlated electrochemical images **(a & c)** and bright field/fluorescence image overlays **(b & d)** of Hep G2 cells previously exposed to 0 μM **(a – b)** and 100 μM **(c – d)** PFOS-supplemented full growth media for 16 hours at 37 °C and 5% CO_2. Hep G2 cells loaded with DCF-DA prior to imaging. Cells imaged in 0.5 mM $FcCH_2OH$ in DPBS. Electrochemical images obtained using a Pt microelectrode tip (r = 5 μm) at +0.5 V vs. Ag/AgCl and a glassy carbon rod counter electrode (r = 1.5 mm); images normalized by $i_{T,\infty}$ when $d \geq 100$ μm. Fluorescence images of ROS indicator, DCF, were obtained at $\lambda_{ex}/\lambda_{em}$ 495/535 nm. The fluorescence images were false colored for visual representation.

Additionally, Hu and co-workers reported a statistically significant decrease in mitochondrial membrane potential as well as variations in antioxidative enzyme activity within Hep G2 cells following a 48-hour exposure to ≥100 μM PFOS.[17] To examine related changes in the cellular redox state over time, Hep G2 cells were exposed to PFOS-supplemented full growth media for 48 hours then electrochemically imaged for 2 hours (**Figure 2**). Cells exposed to PFOS exhibited a higher electrochemical response directly following exposure (**Figure 2f-h**) as well as a relatively higher change in the overall electrochemical response over time compared to the control featured in **Figures 2b-d**. As the electrochemical response increased with respect to time, we inferred an increase in oxidative stress due to bioaccumulation of PFOS and exposure to $FcCH_2OH$. To probe this further, we investigated the mechanism associated with the electrochemical response.

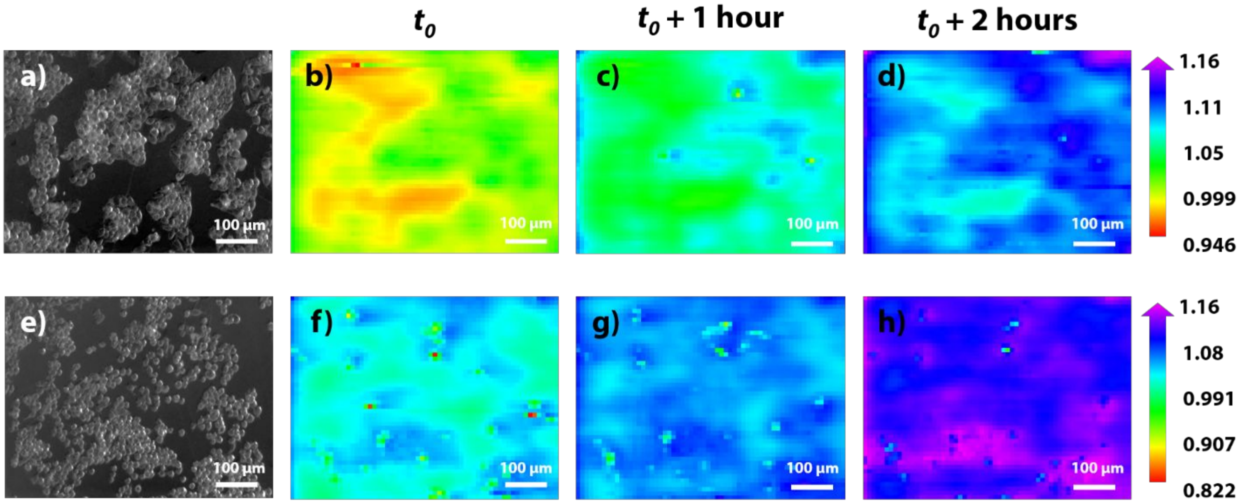

Figure 2. Correlated optical images and electrochemical images of Hep G2 cells previously exposed to 0 µM (**a-d**) and 100 µM (**e-h**) PFOS-supplemented full growth media for 48 hours. Images obtained in 0.5 mM $FcCH_2OH$ in DPBS with a Pt microelectrode tip (r = 5 µm) at +0.5 V vs. Ag/AgCl; a glassy carbon rod was used as the counter electrode (r = 1.5 mm).

Here, it is important to note that PFOS bioaccumulation, local changes in topography[33], and cellular redox activity based on the permeability of $FcCH_2OH$[33] may contribute to the electrochemical response. While electrochemical imaging of cancer cells by oxidation of $FcCH_2OH$ to ferrocenium methanol (Fc^+CH_2OH) has literature precedence[21, 33, 39, 40], the use of $FcCH_2OH$ should not be approached without reservations. $FcCH_2OH$ has been implicated in the upregulation of glutathione (GSH) due to oxidative stress (*i.e.,* an imbalance in ROS production and accumulation in the cell versus antioxidant activity[41]) induced upon entrance into the cell.[40] This upregulation to maintain cellular homeostasis of ROS is followed by transport of GSH from the cell *via* multi-drug resistant protein 1, which Kuss and co-workers hypothesize to chemically regenerate $FcCH_2OH$ from Fc^+CH_2OH produced at the electrode surface.[40] This mechanism of regeneration is referred to as an E_rC_i' mechanism – a special type of EC mechanism – where an electrochemically reversible redox reaction (E_r) is followed by a chemically irreversible reaction (C_i) that regenerates the initial redox reactant, denoted by the prime symbol (“’”). Here, we initially hypothesized that a similar feedback mechanism (**Scheme 1. GSH Facilitated ET**) is feasible since we electrochemically image Hep G2 cells *via* $FcCH_2OH$ oxidation in feedback mode.

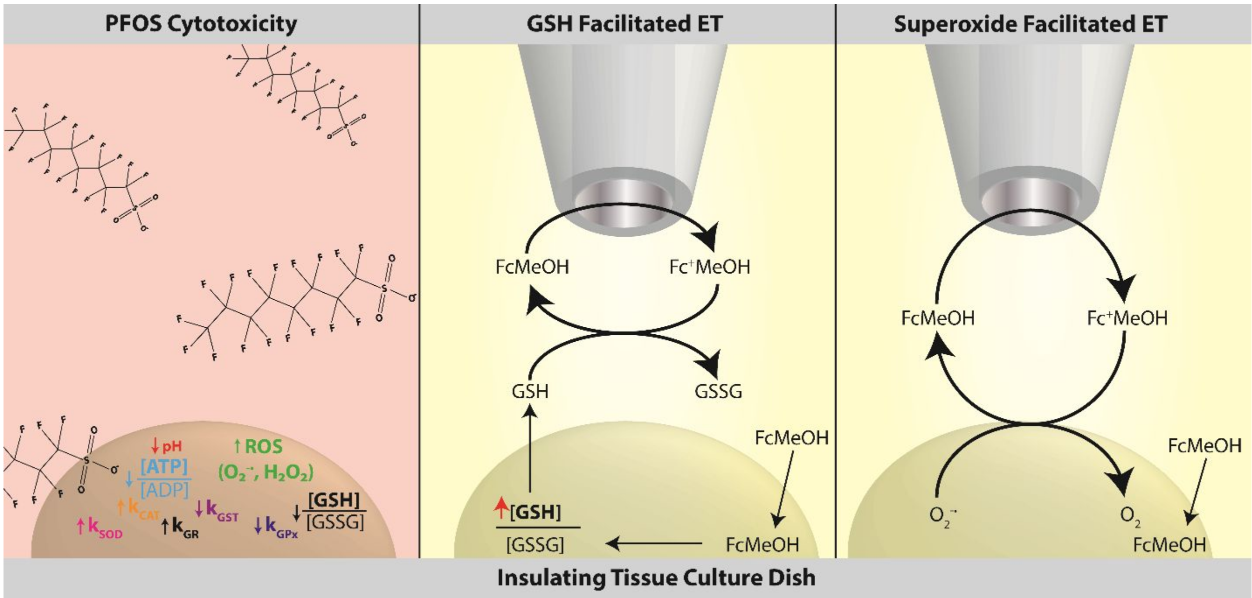

Scheme 1. Schematic representation the mechanism for PFOS cytotoxicity in Hep G2 cells and subsequent possible feedback mechanisms *via* GSH or superoxide anion radical during electrochemical imaging of PFOS-incubated Hep G2 cells by $FcCH_2OH$ oxidation.

To confirm if the E_rC_i' reaction mechanism is feasible, cyclic voltammetry of $FcCH_2OH$ oxidation was performed in the presence of GSH in bulk solution. Similar to the E_rC_i' reaction mechanism corresponding to ferroceniumdimethanol oxidation in the presence of GSH[42], we elucidated an E_rC_i' reaction mechanism in bulk solution using a Pt macroelectrode with $FcCH_2OH$ oxidation to Fc^+CH_2OH followed by the catalytic regeneration of $FcCH_2OH$ in the presence of GSH (**eq. 1 & 2**).

$$FcCH_2OH \leftrightarrow e^- + Fc^+CH_2OH \qquad \textbf{(1)}$$

$$2\,GSH + 2\,Fc^+CH_2OH \rightarrow GSSG + 2\,FcCH_2OH \qquad \textbf{(2)}$$

This is evident in **Figure 3** as the peak current indicative of $FcCH_2OH$ oxidation between +0.20 and +0.30 V vs. Ag/AgCl increases as the GSH concentration in solution increases, while the peak current indicative of Fc^+CH_2OH reduction near +0.18 V vs. Ag/AgCl decreases in magnitude at high concentrations of GSH. We must note that when the concentration of GSH is virtually constant in solution (*i.e.,* when GSH is in excess), the catalytic reaction with ferroceniumdimethanol may be characterized by pseudo-first order kinetics rather than second order kinetics, thus when GSH is in excess (*i.e.,* 4 mM GSH) in the system presented here a significant increase in oxidative current is observed (**Figure 3**).[42]

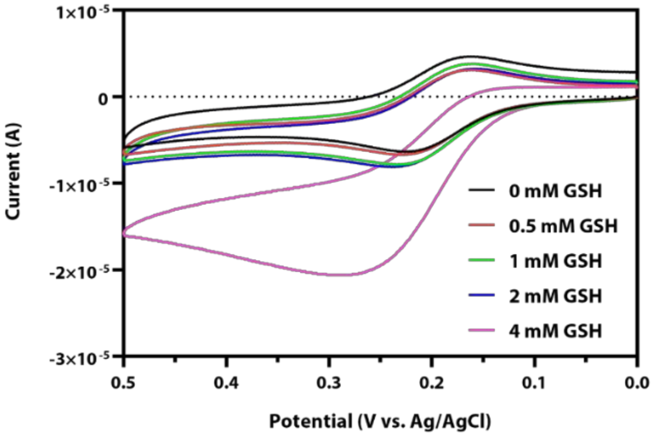

Figure 3. Cyclic voltammograms of 0.5 mM $FcCH_2OH$ combined with 0 mM (black), 0.5 mM (red), 1 mM (green), 2 mM (blue), and 4 mM (pink) GSH in DPBS at a Pt macroelectrode (r = 1 mm) vs. Ag/AgCl after purging each solution for approximately 5 minutes. A glassy carbon rod was used as the counter electrode (r = 1.5 mm).

With cancer cells being equipped with GSH transporters, such as multi-drug resistance proteins, it is more probable for metastatic cells like Hep G2 cells to produce a positive feedback response during electrochemical imaging in the presence of $FcCH_2OH$. Additionally, this feedback mechanism is only feasible due to $FcCH_2OH$ induced oxidative stress. Here, PFOS exposure creates an additional source of oxidative stress. Furthermore, we took additional steps to distinguish between redox mediator induced stress and effects due to PFOS exposure using variable fluorescence bandpass hyperspectral imaging.

We hypothesized that if the feedback mechanism depicted in **Scheme 1. GSH Facilitated ET** were responsible for the positive feedback observed during electrochemical imaging, that extracellular GSH content would increase with respect to PFOS concentration. Therefore, Hep G2 cells were incubated in 0, 50, and 100 µM PFOS-supplemented full growth media for 16 hours, loaded with DCF-DA, and imaged in 0.5 mM $FcCH_2OH$/20µM monochlorobimane (MBCl) in DPBS. These steps were followed to image under similar conditions as used previously to observe the electrochemical response. MBCl was added to solution to conjugate to with GSH in solution, then fluoresce to analyze GSH content (*i.e.,* MBCl is a fluorescence reporter for GSH); this allowed us to determine if extracellular GSH was responsible for the positive feedback response (*i.e.,* to confirm or deny the proposed hypothesis). Contrary to the proposed hypothesis, an increase in GSH content was not a function of PFOS concentration (**Figure 4**), but rather GSH content decreases as PFOS concentration increases. Based on an ordinary one-way ANOVA followed by an unpaired *t*-test, the MBCl-GSH emission intensity decreases significantly from the control using a 95% confidence interval. This significant decrease in GSH content based on MBCl-GSH emission is supported by data collected by Hu and co-workers that reports a decrease in GSH content of lysed Hep G2 cells as function of PFOS exposure.[17] Here, it is important to note that the technique presented allows users to investigate the cellular redox state of living cells *in vitro* opposed to that of lysed cells.

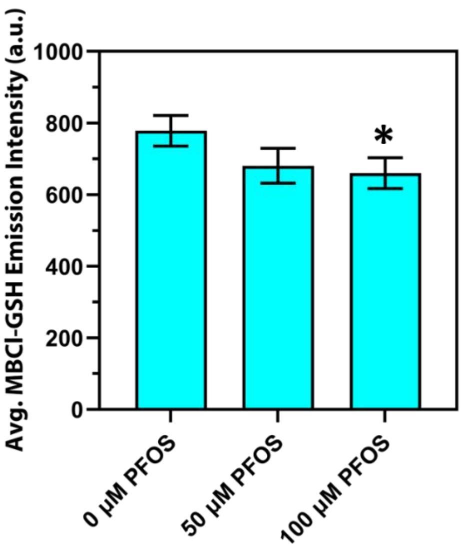

Figure 4. GSH content analysis of Hep G2 cells exposed to PFOS for 16 hours. Hep G2 cells previously loaded with DCF-DA, then imaged in the presence of 0.5 mM $FcCH_2OH$/20 µM MBCl in DPBS. Average MBCl-GSH conjugate emission intensity at $\lambda_{ex}/\lambda_{em}$ 390/490 nm provided as a function of PFOS concentration (*N* = 3). *Significantly different from the control, **p*<0.05.

After using hyperspectral assisted imaging to rule out GSH facilitated electron transfer, reported trends in antioxidative species and enzymes following Hep G2 exposure to PFOS were considered to determine the redox mechanism responsible for the redox state observed *via* electrochemical imaging. Following PFOS exposure, antioxidative enzymes such as superoxide dismutase (SOD), catalase (CAT), and glutathione reductase (GR) increase in activity, while glutathione-*S*-transferase (GST) and glutathione peroxidase (GPx) decrease in activity (**Scheme 1. PFOS Cytotoxicity**); it is important to note, literature precedent for antioxidative enzyme activity is based on manufactured assay kits using lysed cells.[17] With SOD enzyme activity increasing most significantly[17], we hypothesized that electrons lost during the dismutation of superoxide to oxygen by cytoplasmic superoxide dismutase 1 (SOD 1) facilitate the regeneration of FcCH2OH *via* bimolecular electron transfer.

To investigate the role of SOD 1 and superoxide anion radical, Hep G2 cells were treated with a 5 µM solution of a SOD 1 inhibitor (*i.e.,* LCS-1, which is a 2-phenylpyridazin-3(2H)-one based non-copper chelater that selectively inhibits SOD 1 (Cu/Zn-SOD) with IC_{50} = 1.07 µM). Following treatment, the activity of SOD 1 was suspended to prohibit the following mechanism for the dismutation of superoxide (**eq. 3-5**)[43]:

$$Cu^{II}/Zn^{II}SOD\ +\ O_2^{-\cdot} \rightarrow Cu^{I}/Zn^{II}SOD\ +\ O_2 \qquad \textbf{(3)}$$
$$Cu^{I}/Zn^{II}SOD\ +\ O_2^{-\cdot} + 2H^+ \rightarrow Cu^{II}/Zn^{II}SOD\ +\ H_2O_2 \qquad \textbf{(4)}$$

$$2O_2^{-\cdot} + 2H^+ \rightarrow O_2\ +\ H_2O_2 \qquad \textbf{(5)}$$

Upon recognition of a Cu^{II}-redox species, the first reaction mechanism (**eq. 3**) executed by SOD 1 is an outer-sphere electron transfer[43], making it feasible for electrons lost *via* superoxide dismutation to be gained by Fc^+CH_2OH to facilitate the regeneration of $FcCH_2OH$. Alternatively, superoxide anion radicals have been implicated in the regeneration of ferrocene analogs.[44] By suspending SOD 1 activity, we differentiated between these two possible mechanisms.

After inhibiting SOD 1, an increase in the electrochemical response more significant than that of **Figures 1 & 2** was observed in **Figure 5** – where SOD 1 was inhibited by LCS-1 prior to PFOS exposure and imaging – providing evidence for a mechanism in which superoxide anion radicals directly facilitate the bimolecular electron transfer mechanism associated with the positive feedback response as shown in **Scheme 1. Superoxide Facilitated ET**. This mechanism is supported by literature precedent for one-electron reduction of ferrocenium ions *via* superoxide anion radicals.[44, 45]

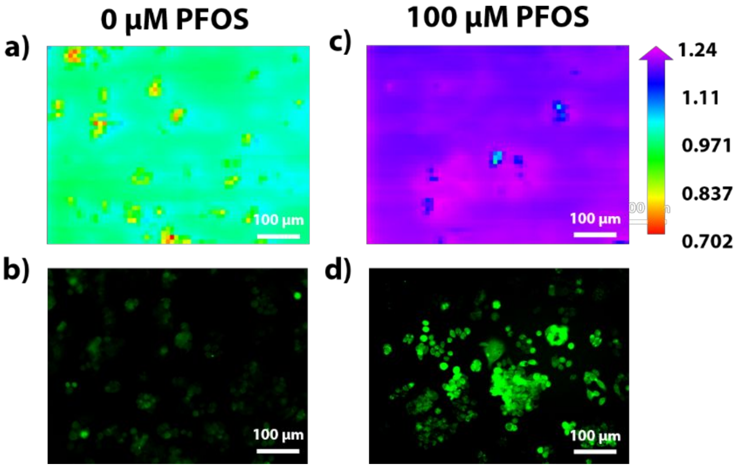

Figure 5. Correlated electrochemical images **(a & c)** and bright field/fluorescence image overlays **(b & d)** of SOD 1 inhibited Hep G2 P28 cells previously exposed to 0 µM (**a – b**) and 100 µM (**c – d**) PFOS-supplemented full growth media for 16 hours at 37 °C and 5% CO_2. Hep G2 cells loaded with DCF-DA prior to imaging. Cells imaged in 0.5 mM $FcCH_2OH$ in DPBS. Electrochemical images obtained using a Pt microelectrode tip (r = 5 µm) at +0.5 V vs. Ag/AgCl and a glassy carbon rod as a counter electrode (r = 1.5 mm); images normalized by $i_{T,\infty}$ when $d \geq$ 100 µm. Fluorescence images of ROS indicator, DCF, were obtained at $\lambda_{ex}/\lambda_{em}$ 495/535 nm. The fluorescence images were false colored for visual representation.

Moreover, H_2O_2 was omitted as a mediator within this bimolecular electron transfer mechanism based on the role of SOD 1 in H_2O_2 production (**eq. 3-5**) and the activity of other antioxidative enzymes. While CAT decomposes H_2O_2, CAT enzyme activity does not increase as significantly as SOD 1 (*i.e.,* <3.2 units per mg compared to SOD 1 when Hep G2 are exposed to 100 µM PFOS and <21.9 units per mg compared to SOD 1 when Hep G2 are exposed to 200 µM PFOS[17]) signifying low dependence on H_2O_2 oxidative stress. Additionally, enzymes responsible for producing additional H_2O_2 like GST and GPx reportedly exhibit decreased enzyme activity due to lack of GSH. Furthermore, superoxide anion radicals are responsible for the increase in cellular reactivity observed following PFOS exposure.

Conclusion

In sum, per- and poly-fluoroalkyl substances (PFAS) are an emerging class of toxic environmental micropollutant. New measurement tools are necessary not only to sense PFAS in the environment[46-50] but to quantify the toxic effect PFAS have on cells. In particular, perfluorooctane sulfonate (PFOS) is one of the most toxic PFAS, and the US Environmental Protection Agency recently lowered the advisory limit down to 10 ppt. In this paper, we used hyperspectral assisted-scanning electrochemical microscope system to investigate the redox mechanism responsible for the electrochemical response of hepatocarcinoma (Hep G2) cells during ferrocenemethanol ($FcCH_2OH$) oxidation following PFOS exposure. The power of using hyperspectral imaging is that spectra can be collected at each pixel, allowing one to precisely investigate spectral intensities and shifts. Specifically, we distinguished between cytotoxic redox mechanisms using redox active-fluorophores and a typical one-electron transfer redox mediator. Following PFOS exposure, a dramatic increase in oxidative current from $FcCH_2OH$-regeneration was accompanied by an increase in dichlorofluorescein fluorescence and a decrease in monochlorobimane-glutathione fluorescence. These results indicate $FcCH_2OH$-regeneration is accompanied by an increase in reactive oxygen species and a decrease in glutathione content. By inhibiting the antioxidative enzyme responsible for the dismutation of superoxide to hydrogen peroxide, we implicated a bimolecular electron transfer mechanism for superoxide facilitated $FcCH_2OH$-regeneration.

As countries continue to establish environmental advisory limits for PFAS, understanding which PFAS have the most deleterious effects on cellular metabolism is imperative. The ability to make such a diagnosis at the single cell level allows one to account for heterogeneities in complex tissues. The method presented in this article for electrochemically monitoring cell metabolism and oxidative stress following PFAS exposure can be used for rapid toxicological screening of different PFAS on different cell lines. Such measurements will begin to inform technological innovations for sensing[46-50], extracting[51, 52], and destroying[53-56] PFAS in the environment.

Conflicts of interest

There are no conflicts to declare.

Acknowledgements

This material is based on work supported by the National Science Foundation Graduate Research Fellowship under Grant No. DGE-1650116. We would also like to acknowledge support from the National Institutes of Health under Grant No. R35-GM138133-01, as well as the University of North Carolina at Chapel Hill for initial startup funds. Additionally, we would like to thank Dr. Matthew Lockett, Dr. Christophe Renault, Dr. Koun Lim, and Lynn Krushinski for helpful discussions.

References

1. Y. Pan, H. Zhang, Q. Cui, N. Sheng, L. W. Y. Yeung, Y. Sun, Y. Guo and J. Dai, *Environ Sci Technol*, 2018, **52**, 7621-7629.

2. Z. Zeng, B. Song, R. Xiao, G. Zeng, J. Gong, M. Chen, P. Xu, P. Zhang, M. Shen and H. Yi, *Environment International*, 2019, **126**, 598-610.
3. D. S. Garcia, M. Sjodin, M. Hellstrandh, U. Norinder, V. Nikiforova, J. Lindberg, E. Wincent, A. Bergman, I. Cotgreave and V. M. Kos, *Chemico-Biological Interactions*, 2018, **281**, 1-10.
4. N. Sheng, R. N. Cui, J. H. Wang, Y. Guo, J. S. Wang and J. Y. Dai, *Archives of Toxicology*, 2018, **92**, 359-369.
5. A. Di Nisio, M. S. Rocca, I. Sabovic, M. D. Ponce, C. Corsini, D. Guidolin, C. Zanon, L. Acquasaliente, A. R. Carosso, L. De Toni and C. Foresta, *Chemosphere*, 2020, **242**, 9.
6. E. M. Sunderland, X. D. C. Hu, C. Dassuncao, A. K. Tokranov, C. C. Wagner and J. G. Allen, *Journal of Exposure Science and Environmental Epidemiology*, 2019, **29**, 131-147.
7. B. N. Conway, A. N. Badders, T. Costacou, J. M. Arthur and K. E. Innes, *Diabetes Metabolic Syndrome and Obesity-Targets and Therapy*, 2018, **11**, 707-716.
8. D. Herzke, E. Olsson and S. Posner, *Chemosphere*, 2012, **88**, 980-987.
9. E. C. Bonefeld-Jorgensen, M. H. Long, S. O. Fredslund, R. Bossi and J. Olsen, *Cancer Causes & Control*, 2014, **25**, 1439-1448.
10. R. R. Worley, S. M. Moore, B. C. Tierney, X. Y. Ye, A. M. Calafat, S. Campbell, M. B. Woudneh and J. Fisher, *Environment International*, 2017, **106**, 135-143.
11. S. Hurley, D. Goldberg, M. M. Wang, J. S. Park, M. Petreas, L. Bernstein, H. Anton-Culver, D. O. Nelson and P. Reynolds, *Environmental Health*, 2018, **17**.
12. K. Kleszczynski and A. C. Skladanowski, *Toxicology and Applied Pharmacology*, 2011, **251**, 163-168.
13. A. F. Ojo, C. Peng and J. C. Ng, *Environmental Pollution*, 2020, **263**, 12.
14. C. E. Rockwell, A. E. Turley, X. G. Cheng, P. E. Fields and C. D. Klaassen, *Food and Chemical Toxicology*, 2017, **100**, 24-33.
15. J. A. Gimenez-Bastida, M. Surma and H. Zielinski, *Toxicology in Vitro*, 2015, **29**, 1683-1691.
16. A. Peropadre, M. J. Hazen, J. M. P. Martin and P. F. Freire, *Environmental Pollution*, 2020, **260**, 9.
17. X. Z. Hu and D. C. Hu, *Archives of Toxicology*, 2009, **83**, 851-861.
18. F. R. Niu, D. C. Wang, J. P. Lu, W. Wu and X. D. Wang, *Journal of Cellular and Molecular Medicine*, 2016, **20**, 1789-1795.
19. C. J. Tape, *Trends in Biotechnology*, 2016, **34**, 627-637.
20. J. B. Robertson, C. R. Davis and C. H. Johnson, *Proceedings of the National Academy of Sciences of the United States of America*, 2013, **110**, 21130-21135.
21. D. Polcari, P. Dauphin-Ducharme and J. Mauzeroll, *Chemical Reviews*, 2016, **116**, 13234-13278.
22. H. K. McCormick and J. E. Dick, *Analytical and Bioanalytical Chemistry*, 2021, **413**, 17-24.
23. F. P. Filice and Z. F. Ding, *Analyst*, 2019, **144**, 738-752.
24. S. Goines and J. E. Dick, *Journal of the Electrochemical Society*, 2019, **167**.
25. Y. Li, J. Lang, Z. Ye, M. Wang, Y. Yang, X. Guo, J. Zhuang, J. Zhang, F. Xu and F. Li, *Analytical Chemistry*, 2020, **92**, 4771-4779.
26. J. Lang, Y. Li, Z. Ye, Y. Yang, F. Xu, G. Huang, J. Zhang and F. Li, *Analytical Chemistry*, 2021, **93**, 5797-5804.
27. J. Mauzeroll and J. Bard Allen, *Proceedings of the National Academy of Sciences*, 2004, **101**, 7862-7867.
28. C. S. Santos, A. J. Kowaltowski and M. Bertotti, *Scientific Reports*, 2017, **7**, 11428.
29. M. Nebel, S. Grützke, N. Diab, A. Schulte and W. Schuhmann, *Angewandte Chemie International Edition*, 2013, **52**, 6335-6338.
30. H. Kikuchi, A. Prasad, R. Matsuoka, S. Aoyagi, T. Matsue and S. Kasai, *Frontiers in Physiology*, 2016, **7**.

31. J. P. Wilburn, M. Ciobanu and D. E. Cliffel, *Journal of The Electrochemical Society*, 2015, **163**, H3077-H3082.
32. Y. Takahashi, I. Shevchuk Andrew, P. Novak, B. Babakinejad, J. Macpherson, R. Unwin Patrick, H. Shiku, J. Gorelik, D. Klenerman, E. Korchev Yuri and T. Matsue, *Proceedings of the National Academy of Sciences*, 2012, **109**, 11540-11545.
33. S. Kuss, D. Polcari, M. Geissler, D. Brassard and J. Mauzeroll, *Proceedings of the National Academy of Sciences*, 2013, **110**, 9249.
34. S. Goines, M. Deng, M. W. Glasscott, J. Leung and J. E. Dick, *Analyst*, 2022.
35. W. M. A. Westerink and W. G. E. J. Schoonen, *Toxicology in Vitro*, 2007, **21**, 1592-1602.
36. D. Li, L. Jiang, Y. Hong and Z. Cai, *Environmental Pollution*, 2021, **268**, 115774.
37. I. Beaulieu, S. Kuss, J. Mauzeroll and M. Geissler, *Analytical Chemistry*, 2011, **83**, 1485-1492.
38. Z. Nova, H. Skovierova, J. Strnadel, E. Halasova and A. Calkovska, *International Journal of Molecular Sciences*, 2020, **21**, 1148.
39. P. Sun, F. O. Laforge, T. P. Abeyweera, S. A. Rotenberg, J. Carpino and M. V. Mirkin, *Proceedings of the National Academy of Sciences of the United States of America*, 2008, **105**, 443-448.
40. S. Kuss, R. Cornut, I. Beaulieu, M. A. Mezour, B. Annabi and J. Mauzeroll, *Bioelectrochemistry*, 2011, **82**, 29-37.
41. D. J. Betteridge, *Metabolism*, 2000, **49**, 3-8.
42. M. Davceva, V. Mirceski and S. Komorsky-Lovric, *International Journal of Electrochemical Science*, 2011, **6**, 2718-2729.
43. R. C. Maji, P. P. Das, S. Mishra, A. Bhandari, M. Maji and A. K. Patra, *Dalton Transactions*, 2016, **45**, 11898-11910.
44. B. A. Aderibigbe and H. E. Mukaya, in *Nano- and Microscale Drug Delivery Systems*, ed. A. M. Grumezescu, Elsevier, 2017, pp. 33-48.
45. M. Hayyan, M. A. Hashim and I. M. AlNashef, *Chemical Reviews*, 2016, **116**, 3029-3085.
46. P. J. Kauffmann, N. A. Park, R. B. Clark, G. L. Glish and J. E. Dick, *ACS Measurement Science Au*, 2022, **2**, 106-112.
47. R. B. Clark and J. E. Dick, *ACS Sensors*, 2020, **5**, 3591-3598.
48. R. Kazemi, E. I. Potts and J. E. Dick, *Analytical Chemistry*, 2020, **92**, 10597-10605.
49. R. B. Clark and J. E. Dick, *Chemical Communications*, 2021, **57**, 8121-8130.
50. M. W. Glasscott, K. J. Vannoy, R. Kazemi, M. D. Verber and J. E. Dick, *Environmental Science & Technology Letters*, 2020, **7**, 489-495.
51. E. Kumarasamy, I. M. Manning, L. B. Collins, O. Coronell and F. A. Leibfarth, *ACS Central Science*, 2020, **6**, 487-492.
52. R. Ranaweera, C. Ghafari and L. Luo, *Analytical Chemistry*, 2019, **91**, 7744-7748.
53. Z. Sun, C. Zhang, L. Xing, Q. Zhou, W. Dong and M. R. Hoffmann, *Environmental Science & Technology*, 2018, **52**, 2953-2962.
54. S. Hao, Y.-J. Choi, B. Wu, C. P. Higgins, R. Deeb and T. J. Strathmann, *Environmental Science & Technology*, 2021, **55**, 3283-3295.
55. G. K. Longendyke, S. Katel and Y. Wang, *Environmental Science: Processes & Impacts*, 2022, **24**, 196-208.
56. J. Cui, P. Gao and Y. Deng, *Environmental Science & Technology*, 2020, **54**, 3752-3766.